Computational Analysis of a Multiple-Nozzle Supersonic Retropropulsion Configuration

Justin A. Shafner*
University of Maryland, College Park, MD, 20740, USA

Ashley M. Korzun†
NASA Langley Research Center, Hampton, VA, 23681, USA

Supersonic retropropulsion is an enabling capability to land large payloads on the surface of Mars. The retropropulsion flowfield is a highly dynamic environment with strong shocks, free shear layers, and plumes opposing high-speed flow. For flight vehicles with large aerodynamic surface area, such as NASA concepts for human Mars exploration, retropropulsion can induce significant aerodynamic interference forces and moments on the vehicle during powered flight. A multiple-nozzle configuration from upcoming, inert gas, sub-scale, supersonic wind tunnel testing is simulated at Mach 2.4 conditions for angles of attack of 0 and 10 degrees and thrust coefficients of 0.5, 1.0, and 2.5. This paper examines changes in the resulting flowfield, surface pressures, and integrated forces with thrust force coefficient and angle of attack using a Detached Eddy Simulation approach.

I. Nomenclature

A	area, m^2
C	force or moment coefficient
c_p	pressure coefficient
L/D	lift-to-drag ratio
M	Mach number
P	pressure, Pa
q	dynamic pressure, Pa
Re	Reynolds number
T	temperature, K
V	velocity, m/s
α	angle of attack, deg
μ	turbulent viscosity, Pa-s

superscripts/subscripts

0	total condition
2	post-shock condition
A	axial force
e	nozzle exit condition
j	jet condition
My	pitching moment
T	thrust
∞	freestream condition
$*$	nozzle throat condition

II. Introduction

Human exploration of Mars has been a goal since the start of the American space program. NASA has identified sending humans to Mars as a challenge to be accomplished in the next two decades [1]. Human missions to Mars will require the development of new entry, descent, and landing (EDL) vehicles capable of landing payloads an order of magnitude larger than any of the nine successfully landed to date [2–4]. Over the past decade, NASA has renewed work on Supersonic Retropropulsion (SRP), or the initiation of powered descent at supersonic speeds with continuous deceleration through to touchdown, with the target application to human Mars exploration. SRP will be the successor to the Viking-derived supersonic parachute system used to land robotic missions such as Mars Science Laboratory and Mars2020 [5, 6]. The most recent human Mars architecture study update completed by NASA has chosen two likely candidate vehicles for high-mass Mars missions that implement SRP for descent and landing [4]. Figure 1 shows the EDL concept of operations for human-scale low lift-to-drag (L/D) ratio and mid-L/D Mars landers with SRP. These conceptual vehicles initiate retropropulsion between Mach 2.5 and 2.0 and use the main propulsion system not only for

*Graduate Research Assistant, Department of Aerospace Engineering, University of Maryland, College Park, AIAA Member.
†Aerospace Engineer, Atmospheric Flight and Entry Systems Branch, M/S 489, Senior Member AIAA.

deceleration, but also for guidance and control along the flight path to a soft, on-target landing. The low-L/D vehicle delivers a 20 t payload to the surface of Mars using a 16.4 m-diameter hypersonic inflatable aerodynamic decelerator and SRP, and a wind tunnel model based on this conceptual vehicle geometry is the focus of the analysis in this paper.

Propulsive descent initiated at supersonic conditions contains flow phenomena from both traditional blunt-body aerodynamics and free-jet flow. Historically, it has been generally assumed that only propulsive forces affect the decelerating vehicle once the engines are operational. However, results from 2010 supersonic wind tunnel testing demonstrated up to a 5% contribution of aerodynamic forces on vehicle deceleration [7], and computational fluid dynamics (CFD) analyses in recent years predict the potential for an even greater aerodynamic contribution to deceleration [8]. Furthermore, plume-plume interactions and multi-plume-to-freestream interactions present in configurations with multiple nozzles add complexity and significant unsteadiness to the flowfield, increasing the potential for effects that challenge the stability and control of the vehicle [7, 9–14].

Capturing relevant physics for retropropulsion at supersonic conditions will require the combination of wind tunnel testing, flight testing, and CFD analysis. Ground tests provide critical validation data to improve the fundamental understanding of SRP flow physics and to evaluate the uncertainty in prediction of retropropulsion-induced environments with CFD. Once satisfactory agreement is reached between experimental wind tunnel data and CFD simulations, computational approaches can begin to be extended to predict interference effects and environments on larger, more complex and realistic systems. Flight test data will be critical to verify scaling and real-gas effects in preparation for mission infusion applications with realistic Martian atmosphere conditions and engine exhaust.

This paper presents pre-test CFD analyses for a low-L/D vehicle configuration to be tested in an upcoming (2021) SRP wind tunnel test campaign, as well as exploration of the sensitivity of flowfield geometry and unsteady behavior to turbulence modeling. Section III presents an overview of the upcoming wind tunnel test and forthcoming data products. Section IV.A describes the computational modeling and simulation approach applied in this analysis. Section V provides a survey of the CFD simulation results highlighting main characteristics of the different flow solutions. Section VI discusses further analysis and comparisons with expected outcomes from the upcoming wind tunnel test.

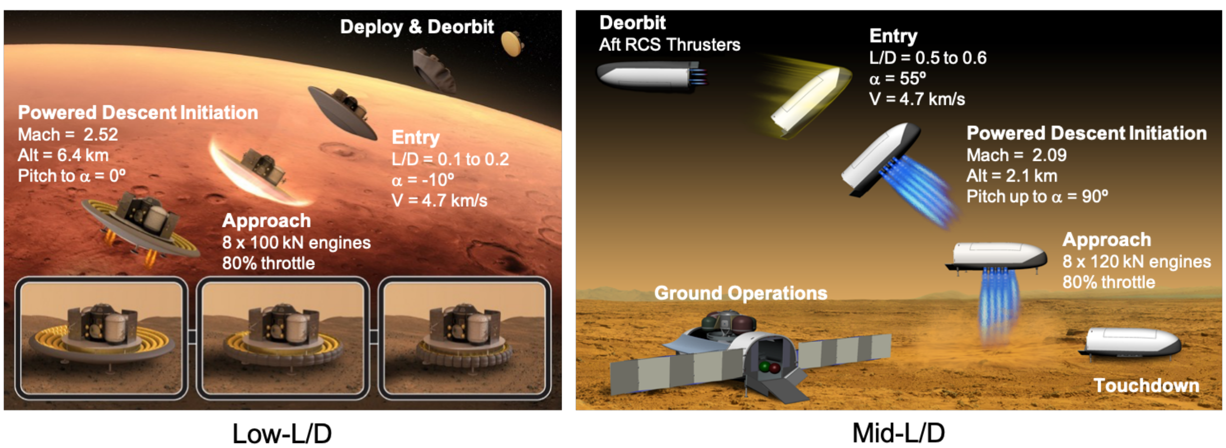

Fig. 1 Conceptual low-L/D (left) and mid-L/D EDL vehicles for human Mars exploration [15].

III. Wind Tunnel Test Summary

The 2021 SRP test campaign will be conducted in Test Section 2 of the NASA Langley Unitary Plan Wind Tunnel, a closed-circuit, continuous-flow pressure tunnel with two nominal 4-foot × 4-foot test sections. The existing high-pressure air capability, supersonic freestream conditions from 2.30 to 4.63 in Test Section 2, and optical access are well-suited for subscale, inert gas testing of SRP. This test section was used previously for the 2010 SRP wind tunnel test efforts [16]. The objective of the 2021 SRP wind tunnel test campaign is to generate SRP data for the evaluation of predictive computational capabilities using sub-scale, realistic Mars landing vehicle configurations with inert gas (air) engine exhaust plume simulant. Sub-scale models of low-L/D (see Fig.1 for the full-scale concept) and mid-L/D conceptual vehicles will be tested with various nozzle configurations and operating conditions at freestream Mach numbers from 2.4 to 4.6.

This test campaign builds upon the 2010 SRP testing that studied generic SRP flow structures for single and multi-nozzle configurations [16]. At each freestream Mach number condition, thrust force coefficient (C_T) and vehicle attitude will be varied. Flowfield structure and behavior will be captured using high-speed Schlieren video, and surface pressure distributions will be obtained with fixed static pressure taps and high-frequency Kulite measurements, as well as pressure sensitive paint on the model forebody, or heatshield. Direct force and moment measurements are to be attempted for the first time with a subset of runs in this test using a new 6-component, flow-through wind tunnel balance.

A. Model Geometry

Of the six low-L/D models to be tested, this computational study focuses on the configuration with a semi-peripheral arrangement of eight supersonic, axially-aligned, conical nozzles scarfed to be flush with the forebody. The model forebody, or heatshield, is 5 inches in diameter. The nozzle area ratio, A_e/A^*, of each unscarfed nozzle is 4, yielding an ideal exit Mach number, M_e of 2.94. The nozzles have a 0° cant angle, meaning that they point forward, parallel to the heatshield's axis of symmetry. Figure 2 shows views of the model forebody (left), model components (middle), and nozzle internal flow path (right). The eight nozzles are visible in the forebody view, in an equally-spaced configuration at the model half-radius. The red dots in Fig. 2 indicate the locations of static pressure taps. In addition to the nozzle and configuration shown in Fig. 2, other nozzles will be tested to obtain data on the effects of nozzle cant angle, area ratio, size, and location on the heatshield.

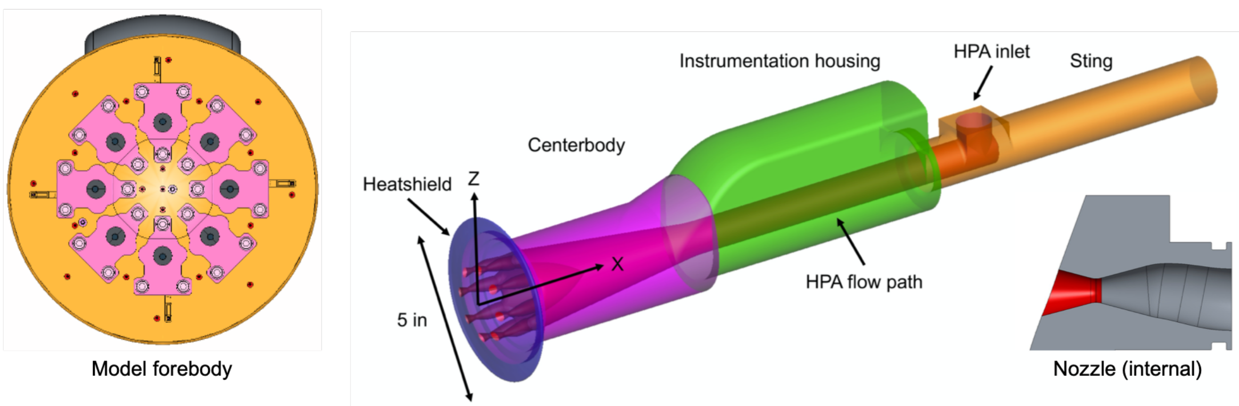

Fig. 2 Forebody (left), model components (center), and internal nozzle flow path (right) views of the wind tunnel model configuration with eight equally-spaced nozzles at the forebody half-radius.

B. Run Conditions Summary

Table 1 lists the conditions simulated in this study. All cases are at an M_∞ of 2.386 and a Re_∞ of 1×10^6 per foot. Angles of attack of 0° and 10° are evaluated for each C_T. The pressure ratio, $P_e/P_{0,2}$, ranges from less than unity to greater than unity, where a single nozzle is considered. Prior work has established this ratio as indicative of an over-expanded ($P_e/P_{0,2} < 1$) or an under-expanded ($P_e/P_{0,2} > 1$) nozzle flow, where the post-shock freestream stagnation pressure is a reasonable surrogate for the local ambient pressure at the nozzle exit [14].

Table 1 Run Conditions

Freestream Conditions				
M_∞	V_∞ (m/s)	P_∞ (Pa)	$T_{0,\infty}$ (K)	q_∞ (Pa)
2.386	589.5	2527.1	324.8	10069.2

Nozzle Conditions				
C_T	$P_{0,j}$ (kPa)	$T_{0,j}$ (K)	M_e	$P_e/P_{0,2}$
2.5	2130.7	394.3	2.94	3.215
1.0	852.3	394.3	2.94	1.286
0.5	426.1	394.3	2.94	0.643

IV. Computational Approach

A. Run Setup

The Fully Unstructured Navier-Stokes 3D (FUN3D) flow solver is used for all computations, with a long history of application to SRP [8–13, 17]. FUN3D [18] uses a spatially second-order accurate, node-based, finite-volume scheme with implicit time integration. This work uses a steady-state approach with local time-stepping to develop an initial solution before changing to a time-dependent approach. The time-dependent simulations use a temporally second-order accurate approach where each physical time step is treated as a quasi-steady problem. In this analysis, five subiterations per physical time step are used, generally resulting in a 2-to-3 order-of-magnitude drop in the residual history across this interval. Each physical time step advances the flow a distance of 0.0005 m, such that approximately 230 steps are required to travel a distance equal to the heatshield diameter at freestream conditions. The physical time step is 9.25×10^{-7} s. Each of the six cases described by Table 1 (three thrust coefficients, each at two angles of attack) is simulated using a Detached Eddy Simulation (DES) [19] approach with the Spalart-Allmaras (SA) [20] submodel. One case, with $C_T = 2.5$ and $\alpha = 0°$, is also run using a Reynolds-averaged Navier-Stokes (RANS) approach and the SA turbulence model for comparison.

All solutions assume the freestream and nozzle flows to be thermally and calorically perfect gas air. Nozzle flows are simulated using a jet plenum boundary condition, specifying total pressure and total temperature at a subsonic nozzle inflow surface. All other model surfaces are modeled as no-slip adiabatic walls, and the farfield domain boundaries are assumed to be essentially inviscid. No attempt is made in this analysis to model boundary layers on the walls of the wind tunnel test section.

The computational mesh is generated with GridEx [21], a NASA-developed tool linking the solid model geometry and mesh generation, and the Advancing-Front/Local-Reconnection (AFLR3) mesh generation tool [22]. The mesh is mixed-element, with prisms in the boundary layer and tetrahedra in the volume, for a total of 52.1 million grid points. Figure 3 shows a center-cut plane of the grid, depicting the additional volume sourcing used to reduce spacing in the domain near the model, near the nozzle exits, and over the expected shock and plume interference regions. Also visible in Fig. 3 is the model geometry. The surface is smooth and does not include the sting and support structure or high-pressure air supply hardware beyond the end of the instrument housing.

B. Unsteady Turbulence Modeling

CFD comparisons with data from the 2010 NASA wind tunnel test concluded that general flow unsteadiness was highly sensitive to the chosen turbulence model [7]. While dissipative turbulence models such as Spalart-Allmaras result in more steady flow solutions, they do not generally capture all of the appropriate physics in a multi-nozzle SRP flowfield. This section analyzes the highly dissipative turbulence model embedded in Spalart-Allmaras (Fig. 4 left) and compares results generated with the DES turbulence model (Fig. 4 right) in the context of SRP flow structures and the motivation to use more computationally expensive DES. The following results are generated on the same grid, with identical inflow conditions, and FUN3D parameters, with the exception of the turbulence model.

A qualitative comparison of the two instantaneous Mach number contour plots in Fig. 4 show similar characteristics such as plume extent upstream, bow shock displacement, and general Mach numbers throughout the solution. However,

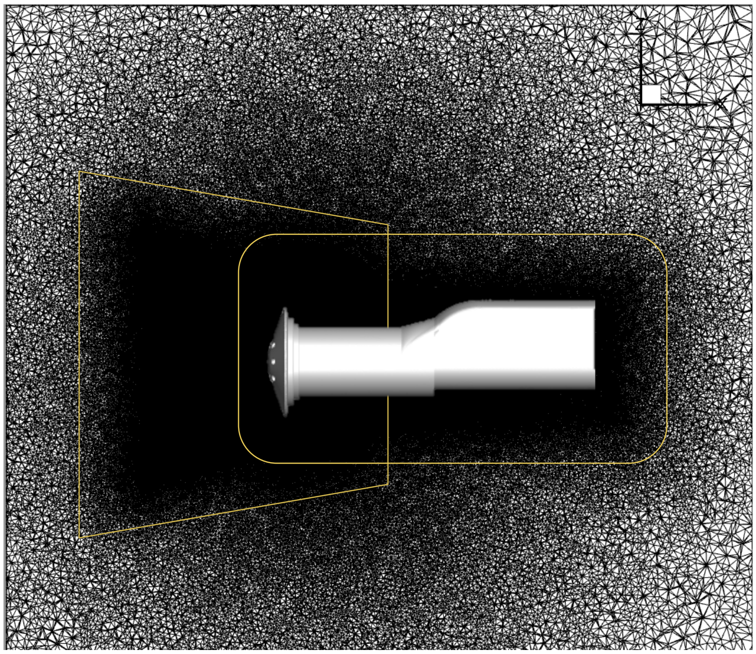

Fig. 3 Near-model view of the computational mesh with volume sourcing.

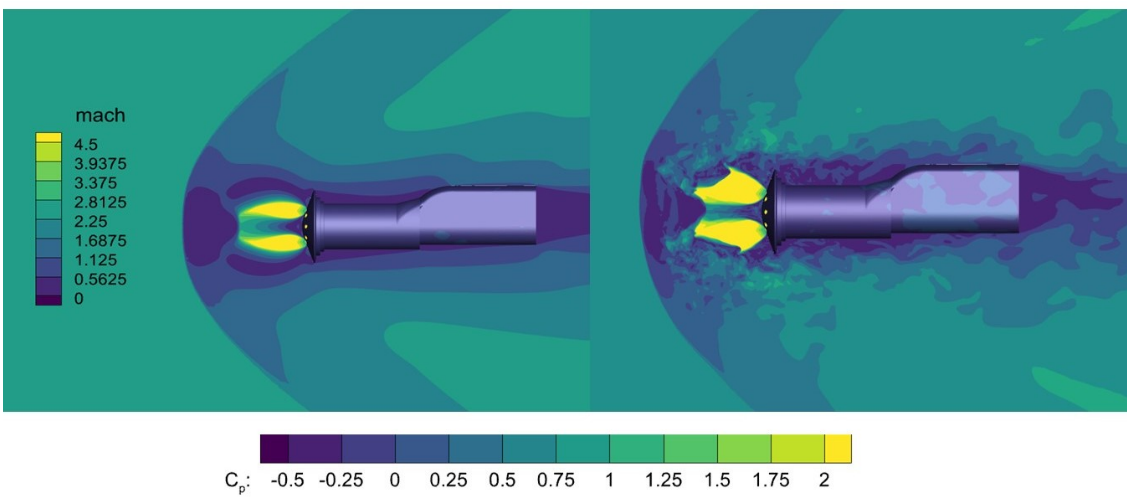

Fig. 4 Instantaneous Mach number and surface c_p contour for C_T = 2.5 using the Spalart-Allmaras (left) and DES (right) turbulence model.

it is clear that the DES solution exhibits highly unsteady flow, while the SA turbulence model solution has much more stationary flow characteristics. It is difficult to discern through an instantaneous snapshot, but the SA flow solution remains largely unchanged after more than 5000 time steps with a continually converging residual history. In comparison, the unsteady flow solution from the DES case settles to a fluctuating residual state expected for time-varying flow. Both previous CFD simulations and 2010 tunnel test data lead to the expectation that the eight-nozzle configuration will have highly turbulent, unsteady flow, rather than the steady flow observed using the SA turbulence model [16]. This non-physical steady-state solution is a byproduct of attempting to implement Spalart-Allmaras turbulence models in regions where the mathematical model departs from physical accuracy.

The usefulness and computationally efficient utilization of single equation Spalart-Allmaras turbulence models have made them an ideal choice for resolving large flow fields and complex turbulence solutions. The accuracy of SA turbulence models for wall-bounded flow is well known and well documented [19, 20, 23]. The SA turbulence model relies on a single transport equation for eddy viscosity, ν_t, which governs the magnitude of vorticity in the flow field. The elegant singular equation is used to determine the Reynolds Stress contribution to the Navier Stokes equations through either a linear Boussinesq relationship or modified quadratic relationship. Full derivations and definitions can be found in [20] and [23].

Spalart and Allmaras [23] summarize the SA-neg turbulence model as an accounting equation, shown in Equation (1), where eddy viscosity, ν_t, is related to $\tilde{\nu}$ by a correlation factor. The equation is broken into a production term, P_n, a destruction term, D_n, and a dissipation term. One drawback to this model that applies uniquely to SRP flow fields is the finite, yet large, production of eddy viscosity in jet and wake regions away from the body, forcing an off-body turbulent flow-field to drive towards a steady-state solution. For understanding this phenomenon as it pertains to SRP solutions, the main concernt is with the destruction, D_n, term in Equation (3).

$$\frac{D\tilde{\nu}}{Dt} = P_n - D_n + \frac{1}{\sigma}\nabla \cdot \left[\left(\nu + \tilde{\nu} f_n\right)\nabla\tilde{\nu}\right] + \frac{c_{b_2}}{\sigma}\left(\nabla\tilde{\nu}\right)^2 \tag{1}$$

$$with \quad P_n = c_{b_1}(1 - c_{t_3})S\tilde{\nu} \tag{2}$$

$$and \quad D_n = -c_{w_1}\left[\frac{\tilde{\nu}^2}{d^2}\right] \tag{3}$$

Taking the simple interpretation of viscosity as a fluid's resistance to motion, it is expected that regions of high eddy viscosity will be highly resistant to eddy production and turbulence. In the SA-neg transport equation, the destruction of eddy viscosity is inversely proportional to the square of d, the distance from the nearest wall node. In the case of SRP flow structures, the bow shock and mixing layer are multiple body diameters upstream of the nearest wall node, which effectively sets this destruction term in the eddy viscosity accounting equation to zero. This leads to a large production of eddy viscosity, kept finite and bounded only by the dissipation term. Figure 5 compares the eddy viscosity contours of SA and DES turbulence models at the same iteration presented in Fig. 4. There is an order of magnitude difference in the level of turbulent viscosity around the vehicle between the two cases. The SA case has a thick encasement of viscosity around it that inhibits turbulent vorticity production in the mixing layer, resulting in convergence to steady-state solution. The DES case models less eddy viscosity production in the mixing regions, resulting in highly unsteady and turbulent shear layers, as expected from prior tunnel test data and existing CFD solutions [16].

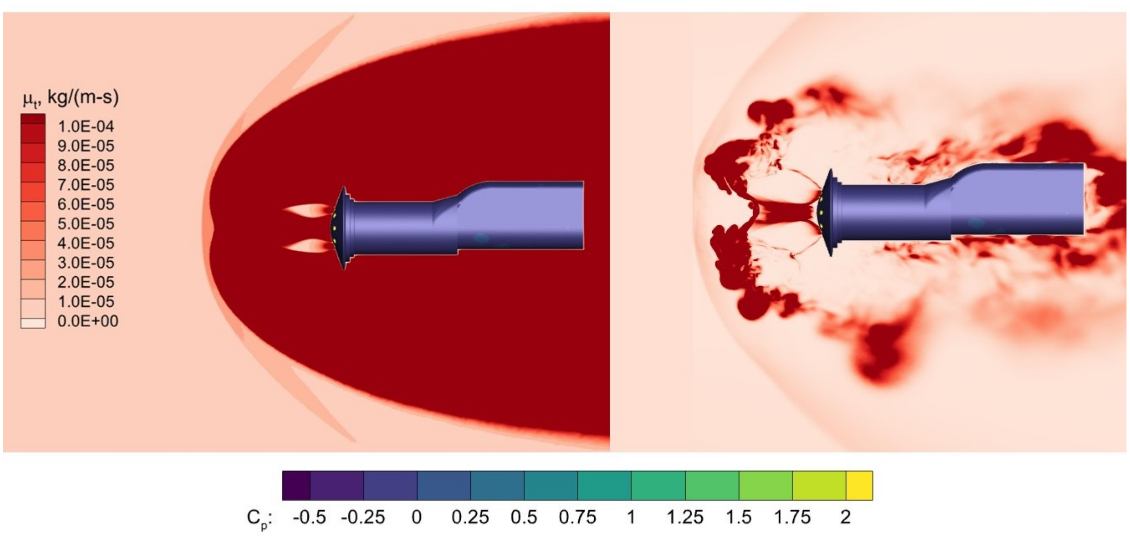

Fig. 5 Instantaneous eddy viscosity contours and surface c_p contours for C_T = 2.5 using the Spalart-Allmaras (left) and DES (right) turbulence model.

The described increase in eddy viscosity remains physically valid for most flow scenarios. In many canonical flow solutions, including blunt-body re-entry, the off-body regions upstream and downstream of the vehicle are typically steady-state, freestream, or quasi-steady wake regions. Therefore, the cascading production of eddy viscosity in these regions maintains physical accuracy when compared to test data. However, the SRP flowfield is unique since it contains highly turbulent mixing regions far from the body. Therefore, the complex turbulence and shock interactions warrant a departure from RANS-based turbulence models and will instead rely on Large Eddy Simulation (LES) modeling. Therefore, the simulations presented here utilize a hybrid DES turbulence model: implementing SA-neg near-wall and LES through the plume, shock, and mixing regions.

V. Results

The upcoming SRP wind tunnel test [15] will gather experimental data on the model shown previously in Fig. 2 at a variety of flow conditions and orientations. The key findings of the time-accurate pre-test CFD solutions outlined in Table 1 are summarized in this section with commentary on observed flow phenomena. The six cases are run for 50,000 time steps using the DES turbulence model as described previously in Section IV.A. Instantaneous slices from each solution are presented in this section as well as time-averaged pressure coefficient. The planar slices are centered through a pair of nozzles. All figures are located at the end of this section. At the time of publication, there are no wind tunnel test data yet available with which to compare these results. Therefore, most analysis provided is qualitative and highlights flowfield differences across the six cases with no commentary on the accuracy as compared to experiment.

A. C_T = 0.5

Figure 6 shows the instantaneous Schlieren, Mach number, and vorticity magnitude contours for the $C_T = 0.5$ case at 50,000 time steps for both $\alpha = 0°$and $\alpha = 10°$. This is the lowest thrust case simulated and exhibits clearly over-expanded plume structures characterized by visible Mach diamonds in the Mach contour plot. The opposing freestream disturbs the jet plumes and causes a radial bending of the jet structures at the displaced bow shock. The vorticity magnitude contours show significant vortex shedding in the mixing region radially surrounding the plumes. In the $\alpha = 10°$case, the freestream further breaks apart the upwind plume, resulting in more flow unsteadiness and a highly turbulent re-circulation stream that flows to the aft of the vehicle.

Further post-processing of the $C_T = 0.5$ case in Fig. 7 shows cold predicted temperatures within the plumes, reaching temperatures as low as 70K. A high pressure region also forms inboard of the nozzles on the heatshield. The forebody pressure coefficient contours represent time-averaged pressure coefficients acting on the vehicle. A clear increase in the aerodynamic forces acting on the upstream portion of the heatshield is observed for the $\alpha = 10°$case. This increase in aerodynamic load is caused by the erosion of the windward portion of the displaced bow shock due to the angled freestream. The flowfield pressure contour shows the high pressure region created by the plumes disturbed by the non-continuous shock structure resulting in a low pressure pocket against the windward region of the heat shield. The relatively small size of the plumes compared to the heatshield frontal area leads to contributions from both propulsive and aerodynamic forces. At this low thrust level, the net coefficient of pressure on the vehicle is positive, or larger than the freestream. For higher thrust cases, where the plumes encompass the entire frontal area of the heatshield, the effects of aerodynamic interference are minimized.

B. C_T = 1.0

Figure 8 shows the instantaneous Schlieren, Mach number, and vorticity magnitude contours for the $C_T = 1.0$ case at 50,000 time steps for both $\alpha = 0°$and $\alpha = 10°$. Mach diamonds are still present, indicating an marginally over-expanded nozzle, but the structures are less perturbed by the opposing freestream due to higher jet thrust momentum. The vorticity magnitude contours show significant vortex shedding around the near-body segments of the plumes with more dissipation away from the body near the bow shock. In the $\alpha = 10°$cases, the directly windward plume exhibits vortex shedding through the entire structure and leads to more unsteady re-circulation to the back of the vehicle. The Schlieren contours indicate that the opposing freestream penetrates the bow shock for the $\alpha = 10°$case, leading to a less defined shock envelope off-body for the windward portion of the vehicle. This behavior was also observed in the lower thrust case ($C_T = 0.5$) and is expected to be a driver of unsteady and potentially non-periodic aerodynamic loads on the heatshield.

Further post-processing of the $C_T = 1.0$ case in Fig. 9 showed extremely cold temperatures in the plumes due to expansion. For the $\alpha = 0°$case, the high pressure region remains attached to the heatshield but extends further into the freestream, leading to a more offset bow shock caused by the stronger plumes. The forebody average pressure coefficient plots indicate similar results to that of $C_T = 0.5$ where aerodynamic interference contributes to the loads on the vehicle in a non-trivial manner. However, the plumes for the $C_T = 1.0$ case are larger and occupy more frontal area than the lower thrust case resulting in less aerodynamic interference in the radial edges of the heatshield. There is still some aerodynamic interference on the body indicated by the noticeable increase in pressure coefficient acting on the windward side of the heat-shield for the α = 10°case. In general, the mixing region of the C_T = 1.0 case appears to be more turbulent than the lower thrust case indicating a very non-uniform thermal mixing region.

C. C_T = 2.5

Figure 10 shows the instantaneous Schlieren, Mach number, and vorticity magnitude contours of the C_T = 2.5 case at 50,000 time steps for both α = 0°and α = 10°. The plume structures for this higher thrust case differ from the previous two in several ways. Clearly under-expanded plume structures are present, and with the increased jet momentum as compared to the prior two cases, these flows are more robust against changes in structure due to the opposing freestream. The mixing region extends not only around the plumes but also upstream of the plumes, introducing significant post-shock turbulence. The bow shock is displaced well beyond the end of the high-speed region of the plumes. The plumes are near steady-state and remain undisturbed by the extended mixing layer or change to the α. Significant vortex shedding is present, with large eddies re-circulating to the aft of the vehicle. For the α = 10°case, the displaced bow shock is not disturbed in the windward portion and remains fully intact. While the level of turbulence is increased by the larger mixing layer compared to the other two lower thrust cases, the near-uniform bow shock and symmetry of the flowfield point to potentially periodic unsteadiness, rather than non-periodic mixing characterized by disruptions to the shock.

The temperature and pressure data for C_T = 2.5 are given in Fig. 11. As evident by the Mach number and vorticity magnitude contours, the mixing layer for the higher thrust case is larger than that observed at the two lower thrust conditions. The entire vehicle and shock region contain highly turbulent thermal mixing layers that recirculate as large boundary layers behind the vehicle. Further, the high-thrust jet-stream displaces the high pressure region away from the heatshield, creating a low pressure buffer between the bow shock and the heatshield. The change in angle of attack minimally impacts this case as evident by the intact bow shock and minor change in pressure distribution across the mixing region. The time-averaged pressure coefficient on the heatshield itself is mostly negative, indicating that there is no positive aerodynamic contribution; vehicle deceleration is entirely propulsive, if not decremented by the aerodynamic interference effects. In addition, only a minor change in pressure coefficient distribution occurs when α is increased to 10°. This suggests that aerodynamic interference contributes less to the overall vehicle load in this case compared to the lower thrust cases. In general, these observations point to a more steady or at least time-periodic turbulence pattern and load acting on the vehicle since both the shock and jet structures appear to be quasi-steady.

D. Force and Moment Time History

Time histories for forces acting on the front surfaces of the heatshield were recorded at each time step throughout the duration of the six simulations. In all cases, these data have been corrected to account for a missing forebody surface section in the original tabulation. An additional 10,000 time steps were run for each case with the full set of forebody surfaces, and the mean of the force and moment history for this individual surface was taken and applied as a correction to the original time history data. Verification of this correction was completed by comparing the means of the corrected, 50,000 time step histories and the additional 10,000 time step histories, and finding a difference of less than 2%. Figure 12 plots the forebody axial force coefficient versus time for both angles of attack and each C_T condition. For the three α = 0°cases, the relative unsteadiness in pressure load acting on the vehicle is small, and the obstruction of post-shock pressure recovery by the plume structure is evident in the marked decrease in C_A with increasing C_T. In the C_T = 2.5 case, the negative value of C_A indicates surface pressures that are lower than the freestream pressure. It should be noted that at these freestream conditions, a pressure increment due to the wake can be non-negligible; any aftbody contribution to axial force is not considered here. In comparing the two angles of attack, the forebody C_A history shows considerably larger oscillations at α = 10° than at α = 0°. Both C_T = 0.5 and C_T = 1.0 exhibit a frequency of approximately 700 Hz. The source of this unsteady effect appears to be the degradation of the bow shock on the windward side as the freestream mixes with the plumes, consistent with angle of attack effects observed in prior wind tunnel testing and CFD analyses [10]. There is only a minor increase in general unsteadiness for the C_T = 2.5 when the angle of attack is increased due to the relative insensitivity of the higher momentum jet structures and overall larger freestream flow obstruction created by the exhaust plumes.

Figure 13 shows the pitching moment coefficient C_{M_y} time history. The moment reference point is the front, center of the model forebody. For the α = 0°cases, a relatively small, but unsteady pitching moment is observed, with a mean generally about zero, with the greatest variation seen in the C_T = 2.5 case. In contrast, a significant pitching moment is observed when α is increased to 10°. The increase in moment in the negative y-direction corresponds to the windward side of the vehicle experiencing more aerodynamic interference than the leeward side. The higher thrust C_T = 2.5 case is less affected by the increase in angle of attack again due to the extent of the obstruction caused by the plume structures. This thrust condition exhibits similar C_{M_y} amplitudes for both α = 0°and α = 10°with only a minor offset from zero for the α = 10°case. The C_T = 0.5 and C_T = 1.0 cases differ more in both amplitude and offset from zero with the increase in angle of attack. There was an increase in unsteady amplitude of roughly an order of magnitude for both cases as well as a distinct shift in mean C_{M_y}. In general, the unsteady oscillations in C_{M_y} are observed to be less periodic than is observed for in the C_A time history for these two thrust conditions.

During the 2010 wind tunnel testing, most of which was conducted at thrust coefficients greater than unity, aerodynamic contributions accounted for less than 5% of the deceleration load on the model. The CFD results presented in this analysis point to a significant contribution to the total deceleration force from aerodynamics as compared to thrust, particularly in the lower thrust cases. Figure 14 shows the relative contributions of thrust and forebody axial force to the total deceleration force in the axial direction. Following the trend from the 2010 tests, the higher thrust coefficients produce less aerodynamic interference, ranging from 5-10%, as much of the available aerodynamic surface aero is obstructed by the plume structures. However, in the lower thrust cases, aerodynamic interference accounts for great than 50% of the deceleration force. As expected, there is generally less aerodynamic interference for the α = 0°cases compared to α = 10°cases.

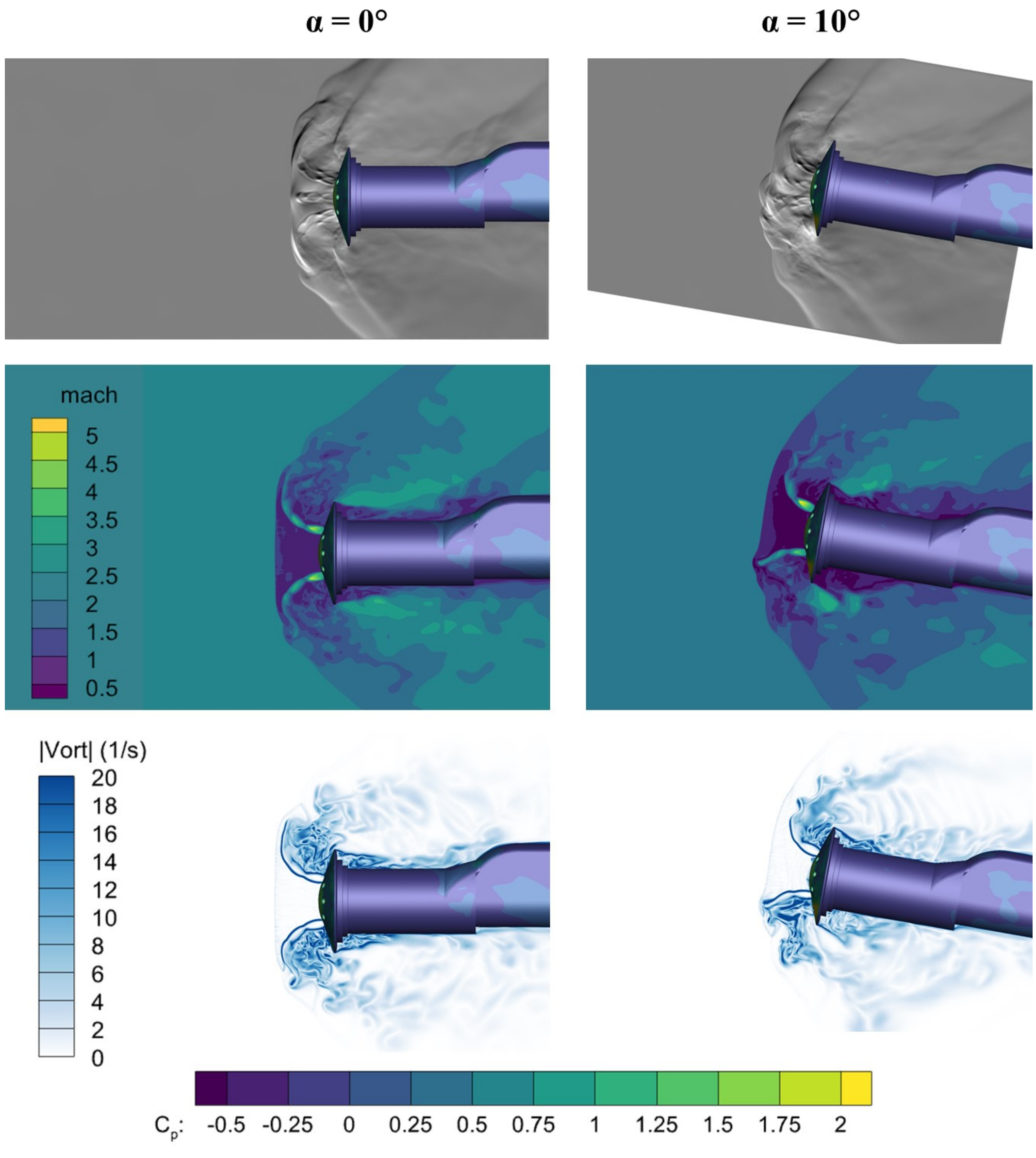

Fig. 6 Instantaneous simulated Schlieren (top), Mach number (mid), and vorticity magnitude (bottom) contours for C_T = 0.5 at 50,000 time steps.

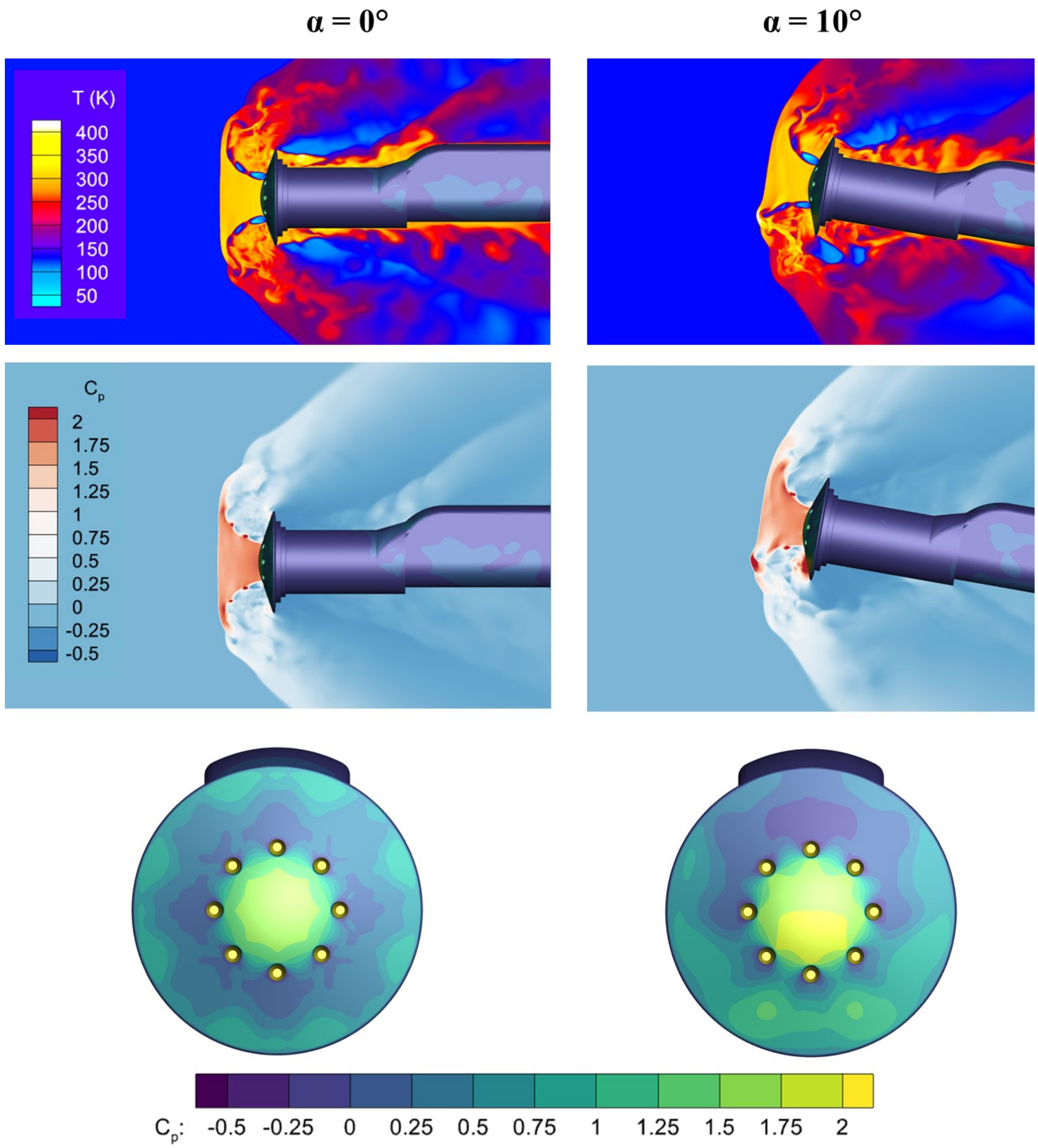

Fig. 7 Instantaneous temperature in Kelvin (top), instantaneous pressure coefficient (mid), and time-averaged pressure coefficient (bottom) plots for C_T = 0.5 over 50,000 time steps.

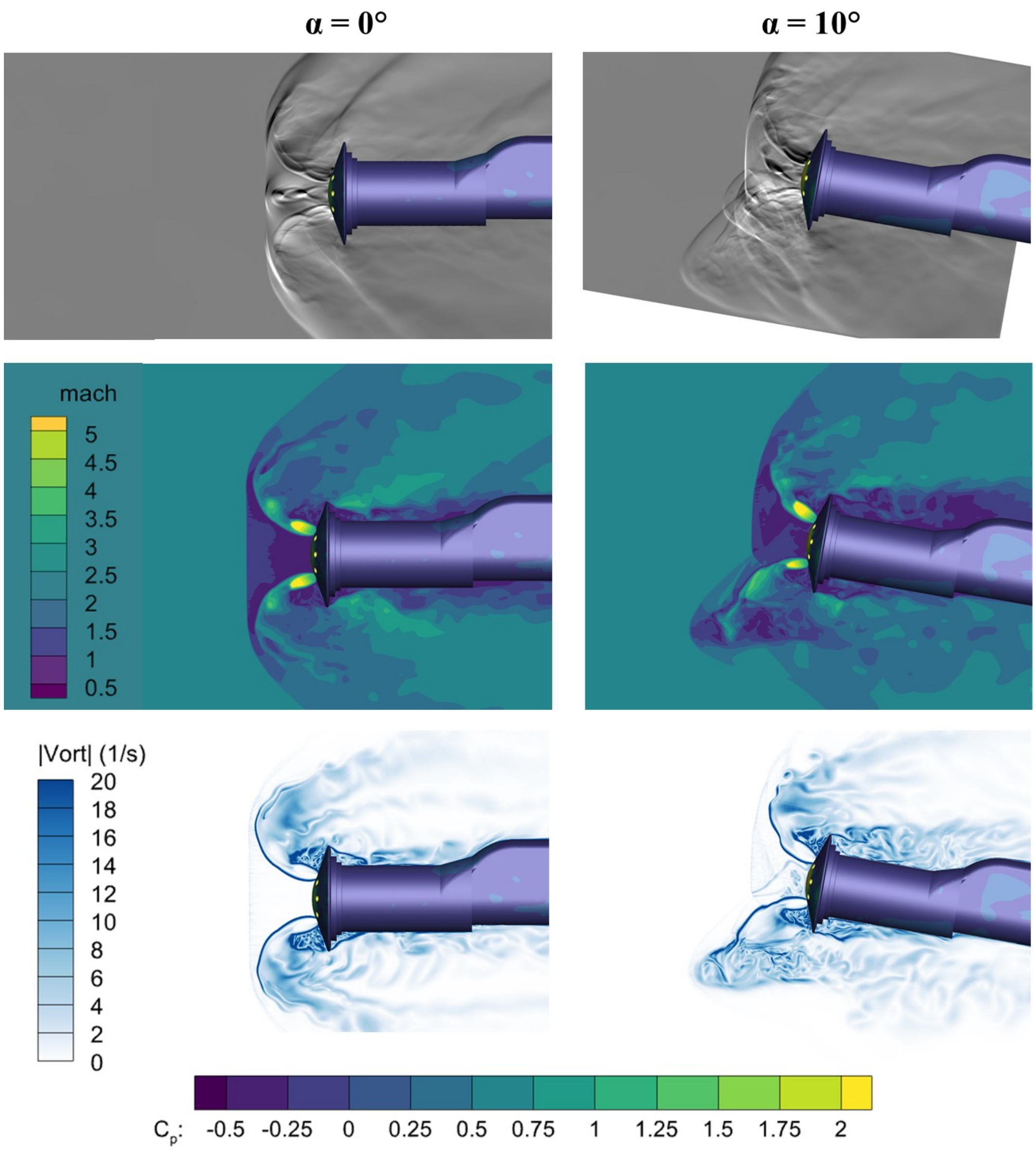

Fig. 8 Instantaneous simulated Schlieren (top), Mach number (mid), and vorticity magnitude (bottom) contours for C_T = 1.0 at 50,000 time steps.

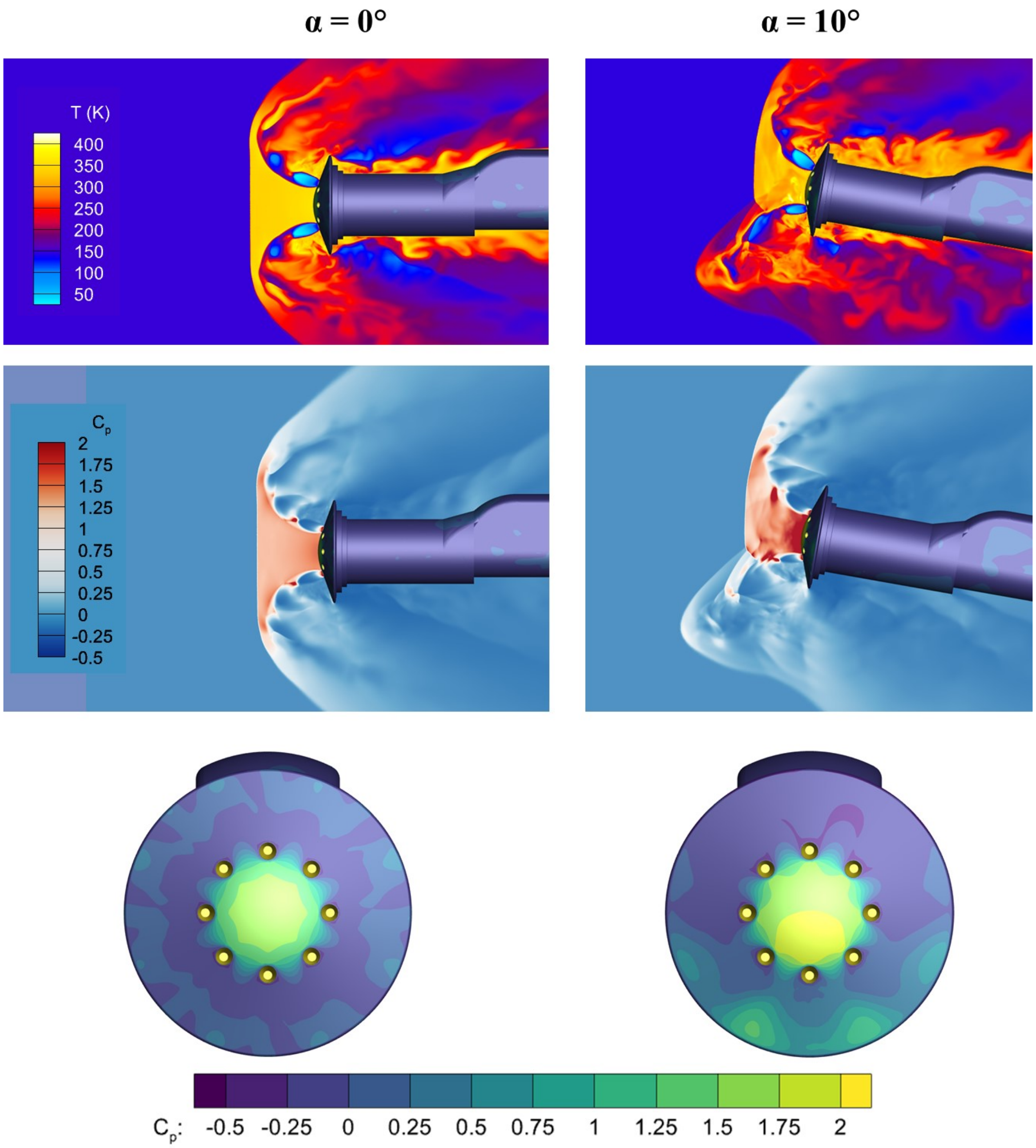

Fig. 9 Instantaneous temperature in Kelvin (top), instantaneous pressure coefficient (mid), and time-averaged pressure coefficient (bottom) plots for C_T = 1.0 over 50,000 time steps.

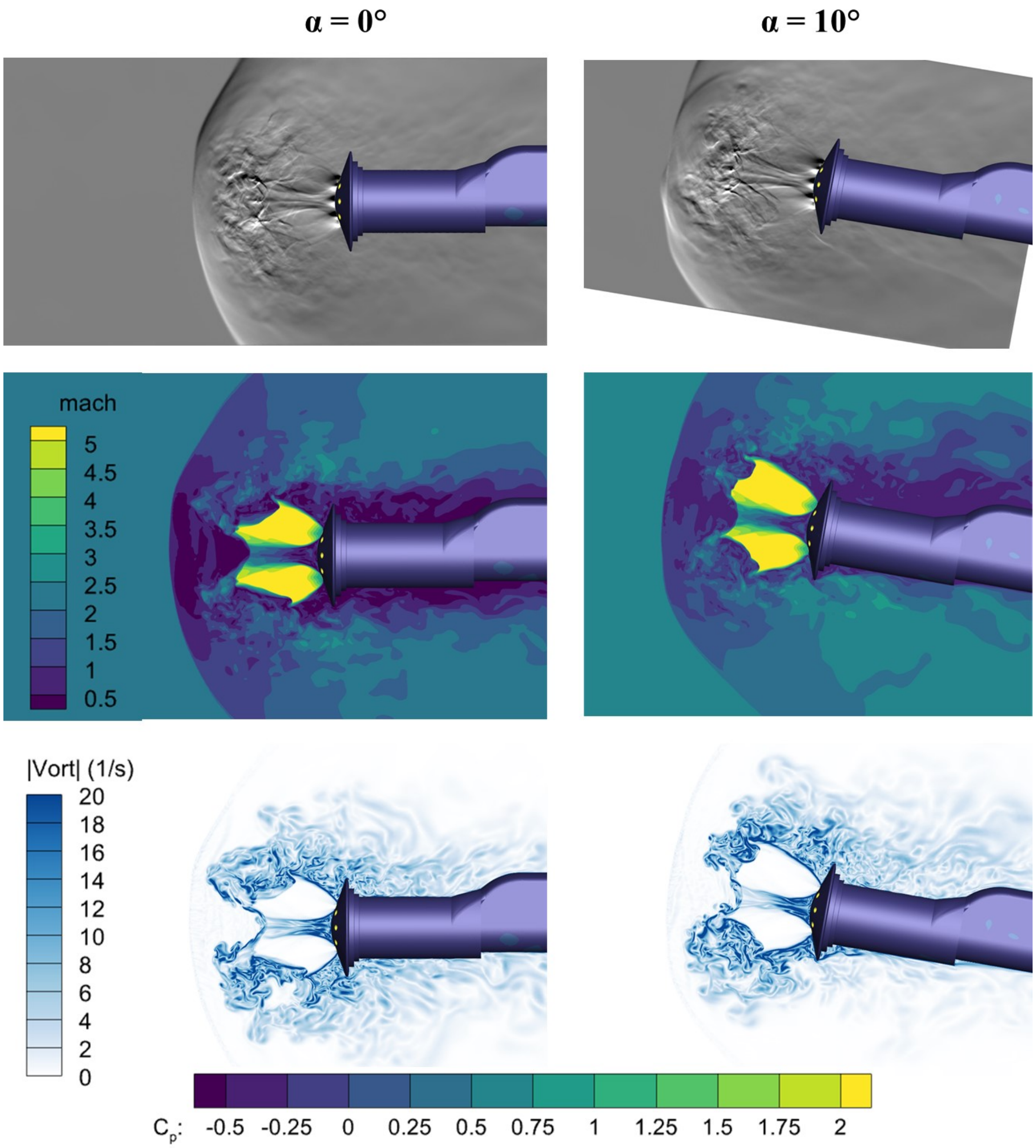

Fig. 10 Instantaneous simulated Schlieren (top), Mach number (mid), and vorticity magnitude (bottom) contours for C_T = 2.5 at 50,000 time steps.

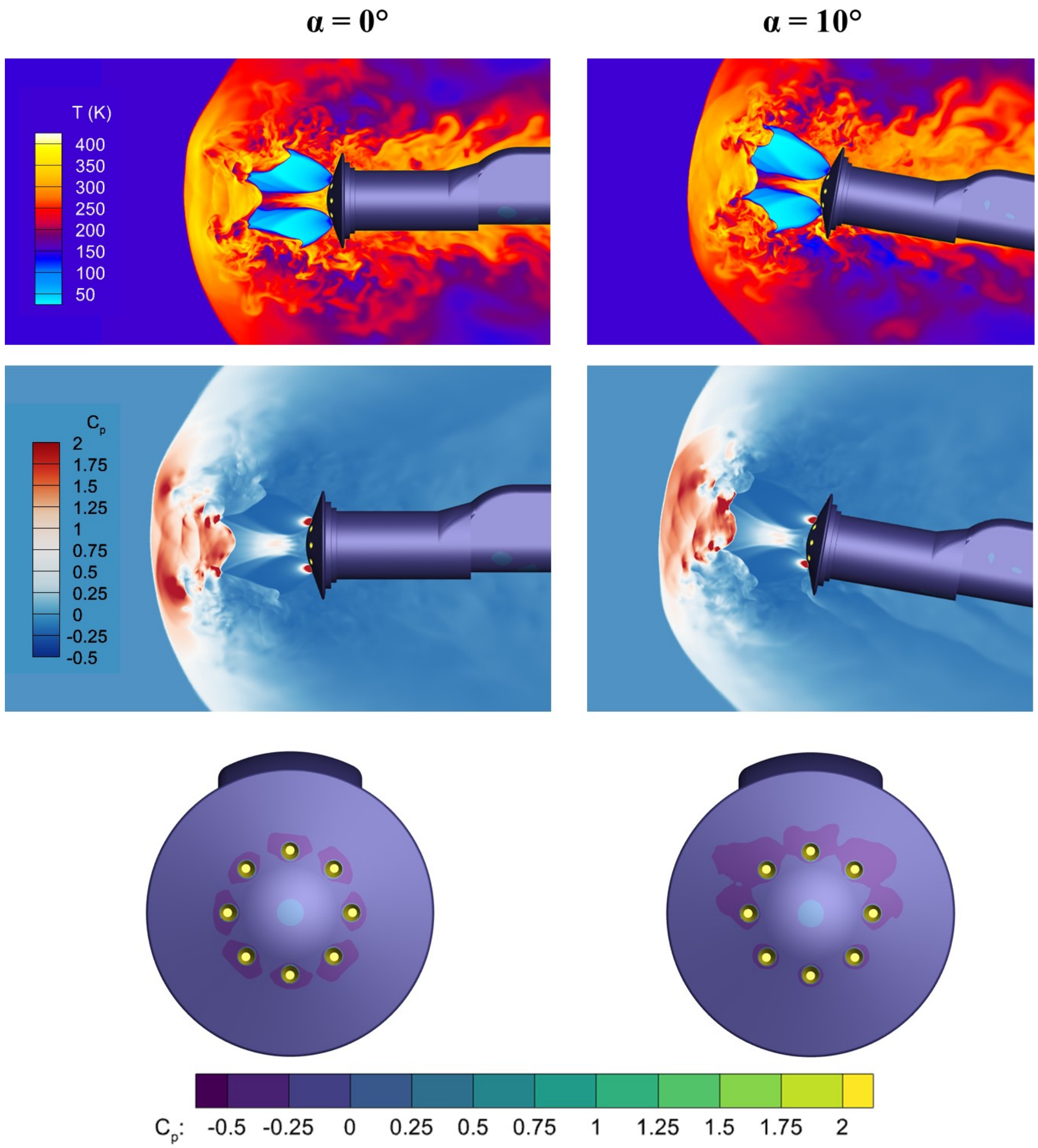

Fig. 11 Instantaneous temperature in Kelvin (top), instantaneous pressure coefficient (mid), and time-averaged pressure coefficient (bottom) plots for C_T = 1.0 case over 50,000 time steps.

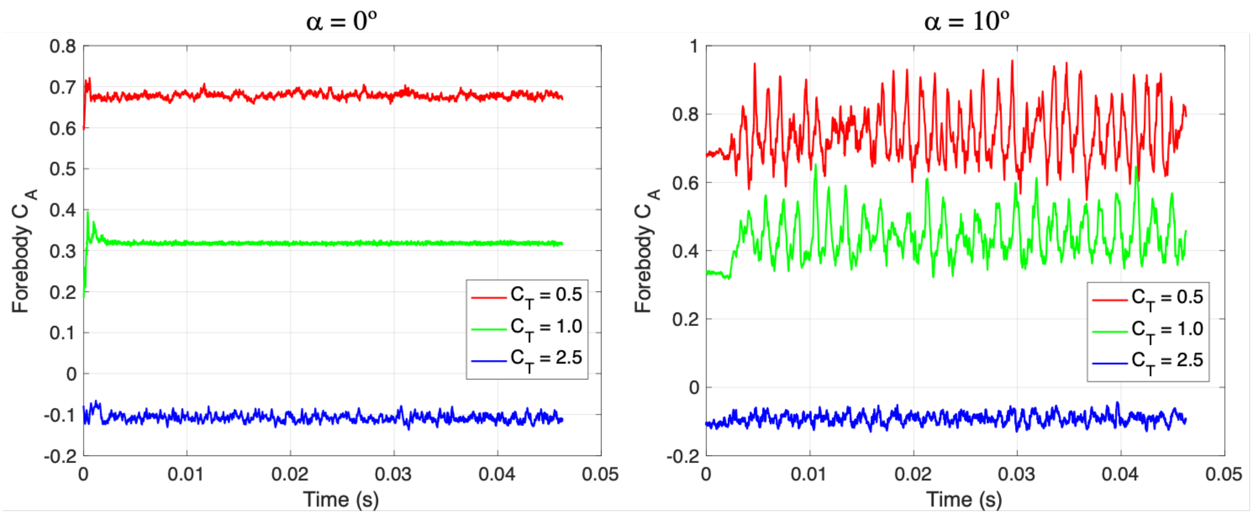

Fig. 12 Time history of forebody axial force coefficient for $\alpha = 0^{\circ}$ (left) and $\alpha = 10^{\circ}$ (right).

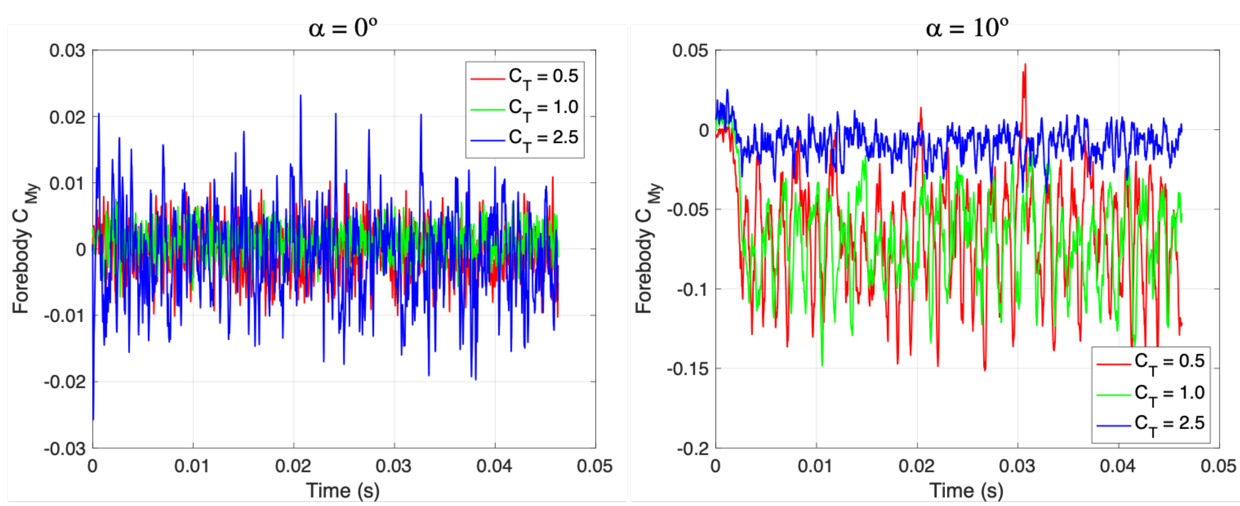

Fig. 13 Time history of forebody pitching moment coefficient for $\alpha = 0^{\circ}$ (left) and $\alpha = 10^{\circ}$ (right).

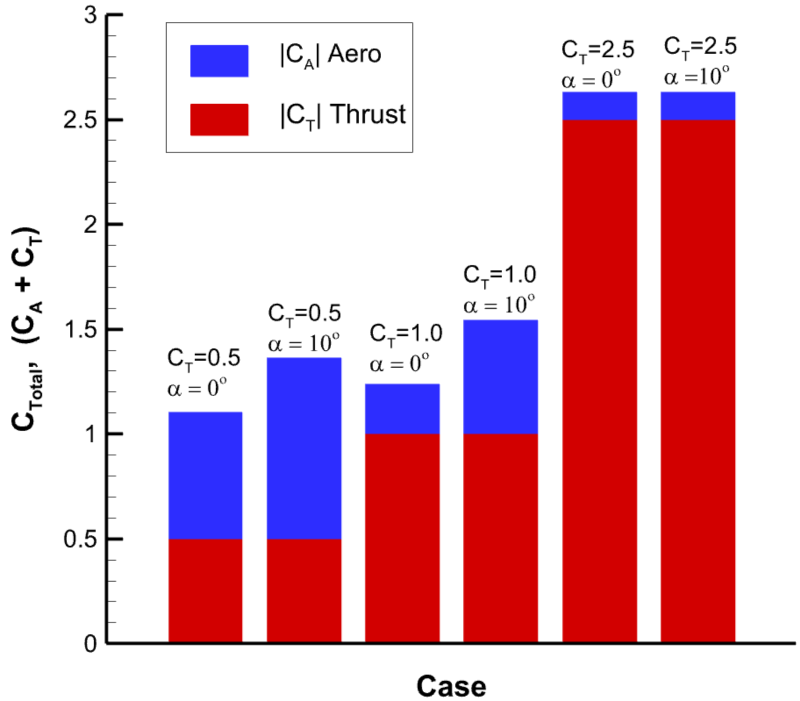

Fig. 14 Forebody total axial force coefficient contributions from aerodynamics and thrust.

VI. Discussion

A. Thrust Coefficient, Angle of Attack, and Plume Structure

The conclusions of the recently published pre-test paper [15] recommend exploring effects of over-expanded plume structures on the unsteady nature of the flowfield. The lowest thrust condition, $C_T = 0.5$, exhibits clearly over-expanded plumes, identified visually by the formation of Mach diamonds in the flow structure. It appears that for both $C_T = 0.5$ and $C_T = 1.0$, the over-expanded plumes extend all the way to the bow shock discontinuity. In these cases, a mixing layer forms radially around the plumes. In contrast, the $C_T = 2.5$ case exhibits a significantly larger bow shock displacement from the heatshield, allowing for both radial mixing layers and a large amount of mixing between the post-shock flow and plume structures. This general trend is further observed in the vorticity magnitude contours. In all six cases considered here, a well-defined mixing region is formed around the plume structures. Large eddies can be seen shedding and recirculating behind the model. It is evident that for the lower $C_T = 0.5$ and $C_T = 1.0$ cases, the opposing freestream more strongly influences the plumes, causing the over-expanded plumes to bend radially outward while shedding into the mixing region. The $C_T = 2.5$ case maintains a normal-to-surface plume structure and significantly more eddy production. As previously mentioned, the higher thrust case has a mixing region behind the shock that generates more vorticity than the lower thrust cases where the bow shock is only displaced to the edge of the plume structures.

The larger bow shock displacement and flow obstruction for the $C_T = 2.5$ case is consistent with the expected result of less overall aerodynamic contributions to the total deceleration force. In the lower-thrust cases, large portions of the heatshield are exposed to the post-shock pressure recovery, but in the highest thrust case, the plumes nearly obstruct the entire frontal area of the heatshield, reducing aerodynamic force magnitudes and flow-mixing on the forebody. This trend is consistent what was observed in the 2010 wind tunnel testing [16], that as thrust coefficient increases beyond unity, the contribution of aerodynamic interference on the model forebody diminishes. For practical vehicle design, these data indicate that the unsteady vehicle effects of the turbulent flowfield are potentially mitigated by adhering to operating conditions where highly under-expanded flow structures are guaranteed.

Further comparisons can be drawn from the Mach number contours to predict different levels of unsteadiness between the $\alpha = 0°$and $\alpha = 10°$cases. In the $C_T = 2.5$ case, the general flowfield in the mixing region is largely unchanged by the increased angle of attack. However, in the weaker plumes of the $C_T = 1.0$ and $C_T = 0.5$ cases, the plumes furthest pitched into the freestream experience more turbulent mixing. This qualitative observation is further illustrated in the vorticity magnitude contours from Section V. The general degree of vortex shedding by the asymmetric plumes is greater than for the $\alpha = 0°$cases. In addition, all three thrust cases exhibit a more robust tripping effect from the pitched heatshield, resulting in slower and more turbulent recirculating boundary layers along the length of the model aft of the heatshield. These simulations modeled the cold air to be used in the upcoming wind tunnel testing. However, in a flight implementation in the Martian atmosphere, these recirculating turbulent flow structures will be comprised of hot combustion products from the main propulsion system. In the flight application, These flow regions could be in non-equilibrium and produce non-negligible heat transfer on and around the vehicle.

B. Forebody Aerodynamic Effects

The main motivation for resolving SRP flowfields is to better understand the aerodynamic interference on the vehicle, primarily on the forebody, which is expected to have the most influential aerodynamic surface area. Understanding uncertainties in the retropropulsion-induced loads on the vehicle will better motivate design decisions for controlling the vehicle through the propulsive descent and landing phases of flight. Both the $C_T = 0.5$ and $C_T = 1.0$ cases show predominantly positive time-averaged c_p values, indicating a positive aerodynamic force contribution to deceleration in addition to the thrust. The high thrust, $C_T = 2.5$ case shows an entirely negative time-averaged c_p indicating very little, if any aerodynamic contribution to forces acting on the heatshield. All three cases with an $\alpha = 10°$show a distinguishable increase in aerodynamic forces on the windward portions of the heatshield when at a non-zero angle of attack. The high thrust, $C_T = 2.5$ case is not as disturbed by the increase in angle of attack as the two lower thrust cases. Both $C_T = 0.5$ and $C_T = 1.0$ exhibit breaks from the radially symmetric pressure distribution of the $\alpha = 0°$cases with a higher pressures observed on the more exposed windward regions of the forebody.

The C_{M_y} results from Figure 13 imply a restorative moment acting on the vehicle when at an angle of attack of 10°pushing the vehicle back to $\alpha = 0°$. Further studies will be needed to evaluate vehicle stability and how the frequency and amplitude of the unsteady moment affect control systems and vibrational modes of the vehicle, especially at the lower thrust coefficients. The upcoming wind tunnel test campaign will gather high-frequency forebody pressure data for much longer time-durations than captured in these CFD simulations and will further characterize these unsteady effects.

VII. Conclusions

This paper presented time-accurate, unsteady, CFD results for six SRP conditions to be tested later in 2021 in the NASA Langley Unitary Plan Wind Tunnel. The results presented indicate highly turbulent, unsteady flow structures with varying degrees of flow complexity and dependence on thrust coefficient and angle of attack. From these findings, the unsteady effects appear to be semi-periodic in nature and oscillating at frequencies in the range of hundreds of Hz. Longer duration CFD simulations and full-duration tunnel tests will further characterize the nature of these oscillations.

A simple, physics-based explanation as to motivating the departure from purely RANS-based CFD for modeling SRP flowfields was outlined through the case of a single equation Spalart-Allmaras turbulence model compared to full DES. It is postulated that most RANS models will be too dissipative to accurately capture the highly turbulent free shear layers and could potentially explain why RANS results generally trend towards more steady solutions. The substantial, parametric, wind tunnel test data generated in the upcoming test will serve as a future validation data source for this work.

Future work will include comparisons of these results with the experimental wind tunnel data to quantify the accuracy of the CFD solutions, especially in the highly turbulent flow regions. Once validation, CFD can begin to extrapolate to design cases such as full-scale flight vehicles for an Earth-based flight test, a hot-fire SRP ground test, or a precursor mission in Martian atmosphere with full combustion propulsion and chemistry in the mixing layers.

References

[1] NASA, “NASA’s Journey to Mars. Pioneering Next Steps in Space Exploration,” NASA NP-2015-08-2018-HQ, October 2015.

[2] Drake, B. G., “Human Exploration of Mars, Design Reference Architecture 5.0 - Addendum,” NASA SP-2009-566-ADD, 2009.

[3] Drake, B. G., “Human Exploration of Mars, Design Reference Architecture 5.0 - Addendum 2,” NASA SP-2009-566-ADD2, 2009.

[4] Dwyer Cianciolo, A. M., Korzun, A. M., Edquist, K. T., Samareh, J., Sostaric, R., Calderon, D., and Garcia, J. A., “Human Mars Entry, Descent, and Landing Architecture Study: Phase 3 Summary,” AIAA Paper 2020–1509, January 2020.

[5] Korzun, A. M., “Design Considerations and Development Status for Atmospheric Powered Descent of High-Mass Payloads at Mars,” IAC Paper IAC-19-A3.3B.13x49535, September 2019.

[6] Edquist, K. T., Korzun, A. M., Dyakonov, A. A., Studak, J. W., Kipp, D. M., and Dupzyk, I. C., “Development of Supersonic Retropropulsion for Future Mars Entry, Descent, and Landing Systems,” *Journal of Spacecraft and Rockets*, Vol. 51, No. 3, 2014, pp. 650–663. https://doi.org/10.2514/1.A32715.

[7] Schauerhamer, D. G., and Trumble, K. A., “Continuing Validation of Computational Fluid Dynamics For Supersonic Retropropulsion,” AIAA Paper 2012–0864, January 2012.

[8] Korzun, A. M., Bibb, K. L., Canabal, F., Childs, R. E., Tang, C. Y., Yehia, M. R., Van Norman, J. W., and Tynis, J. A., “Powered Descent Aerodynamics for Low and Mid Lift-to Drag Human Mars Entry, Descent, and Landing Vehicles,” AIAA Paper 2020–1510, January 2020.

[9] Schauerhamer, D. G., Zarchi, K. A., Kleb, W. L., Carlson, J.-R., and Edquist, K. T., “Supersonic Retropropulsion Computational Fluid Dynamics Validation with Langley 4 x 4 Foot Test Data,” *Journal of Spacecraft and Rockets*, Vol. 51, No. 3, 2014, pp. 693–714. https://doi.org/10.2514/1.A32693.

[10] Schauerhamer, D. G., Zarchi, K. A., Kleb, W. L., and Edquist, K. T., “Supersonic Retropropulsion Computational Fluid Dynamics Validation with Ames 9 x 7 Foot Test Data,” *Journal of Spacecraft and Rockets*, Vol. 51, No. 3, 2014, pp. 735–749.

[11] Zarchi, K. A., Schauerhamer, D. G., Kleb, W. L., Carlson, J.-R., and Edquist, K. T., “Analysis of Navier-Stokes Codes Applied to Supersonic Retropropulsion Wind-Tunnel Test,” *Journal of Spacecraft and Rockets*, Vol. 51, No. 3, 2014, pp. 680–692.

[12] Korzun, A. M., Cordell, C. E., Jr., and Braun, R. D., “Computational Aerodynamic Predictions of Supersonic Retropropulsion Flowfields,” *Journal of Spacecraft and Rockets*, Vol. 50, No. 5, 2013, pp. 950–960.

[13] Korzun, A. M., and Braun, R. D., “Application of a Reynolds-Averaged Navier-Stokes Approach to Supersonic Retropropulsion Flowfields,” *Journal of Spacecraft and Rockets*, Vol. 50, No. 5, 2013, pp. 961–980.

[14] Korzun, A. M., and Cassel, L. A., “Scaling and Similitude in Single Nozzle Supersonic Retropropulsion Aerodynamics Interference,” AIAA Paper 2020–0039, January 2020.

[15] Edquist, K. T., Korzun, A. M., Kleb, B., Hawke, V. M., Rizk, Y. M., Olsen, M. E., and Canabal, F., “Model Design and Pre-Test CFD Analysis for a Supersonic Retropropulsion Wind Tunnel Test,” AIAA Paper 2020–2230, January 2020.

[16] Berry, S. A., Rhode, M. N., and Edquist, K. T., “Supersonic Retropropulsion Validation Experiment in the NASA Langley Unitary Plan Wind Tunnel,” *Journal of Spacecraft and Rockets*, Vol. 51, No. 3, 2014, pp. 664–679.

[17] Korzun, A. M., Nielsen, E. J., Walden, A. C., Carlson, J.-R., Moran, P. J., Henze, C. C., and Sandstrom, T. A., “Effects of Spatial Resolution on Retropropulsion Aerodynamics in an Atmospheric Environment,” AIAA Paper 2020–1749, January 2020.

[18] Biedron, R. T., and et al., “FUN3D Manual 13.6,” NASA TM NASA/TM-2019-220416, 2019.

[19] Spalart, P. R., Deck, S., Shur, M. L., Squires, K. D., Strelets, M. K., and Travin, A., “A New Version of Detached-Eddy Simulation, Resistant to Ambiguous Grid Densities,” *Theoretical and Computational Fluid Dynamics*, Vol. 20, No. 3, 2006.

[20] Spalart, P. R., and Allmaras, S. R., “A One-Equation Turbulence Model for Aerodynamic Flows,” *Recherche Aerospatiale*, Vol. 1, 1994, pp. 5–21.

[21] Jones, W. T., “GridEx – An Integrated Grid Generation Package for CFD,” AIAA Paper 2003–4129, June 2003.

[22] Marcum, D. L., and Gaither, A. J., “Mixed Element Type Unstructured Grid Generation for Viscous Flow Applications,” AIAA Paper 99–3252, June 1999.

[23] Allmaras, S. R., Johnsson, F. T., and Spalart, P. R., “Modifications and Clarifications for the Implementation of the Spalart-Allmaras Turbulence Model,” *ICCFD7*, 2012.